On the Momentum Fluxes Associated with Mountain Waves in Directionally Sheared Flows

MIGUEL A. C. TEIXEIRA AND PEDRO M. A. MIRANDA

CGUL, IDL, University of Lisbon, Lisbon, Portugal

(Manuscript received 7 January 2009, in final form 13 May 2009)

ABSTRACT

The direct impact of mountain waves on the atmospheric circulation is due to the deposition of wave momentum at critical levels, or levels where the waves break. The first process is treated analytically in this study within the framework of linear theory. The variation of the momentum flux with height is investigated for relatively large shears, extending the authors' previous calculations of the surface gravity wave drag to the whole atmosphere. A Wentzel–Kramers–Brillouin (WKB) approximation is used to treat inviscid, steady, nonrotating, hydrostatic flow with directional shear over a circular mesoscale mountain, for generic wind profiles. This approximation must be extended to third order to obtain momentum flux expressions that are accurate to second order. Since the momentum flux only varies because of wave filtering by critical levels, the application of contour integration techniques enables it to be expressed in terms of simple 1D integrals. On the other hand, the momentum flux divergence (which corresponds to the force on the atmosphere that must be represented in gravity wave drag parameterizations) is given in closed analytical form. The momentum flux expressions are tested for idealized wind profiles, where they become a function of the Richardson number (Ri). These expressions tend, for high Ri, to results by previous authors, where wind profile effects on the surface drag were neglected and critical levels acted as perfect absorbers. The linear results are compared with linear and nonlinear numerical simulations, showing a considerable improvement upon corresponding results derived for higher Ri.

1. Introduction

Mesoscale mountains interact with the large-scale atmospheric circulation through the momentum fluxes they produce. Since the troposphere is generally stably stratified, for sufficiently large mountains, a major fraction of these fluxes are caused by the generation of internal gravity waves. At the surface, these gravity waves produce a pressure drag on the mountains. By Newton's third law of motion, a reaction force must be exerted by the mountains on the atmosphere. This reaction force corresponds to the divergence of the momentum flux, which, in the linear approximation (by Eliassen–Palm's theorem), is only nonzero at critical levels (for unidirectional flow) (Eliassen and Palm 1960) or critical layers (in directionally sheared flow) (Broad 1995). These physical processes must be parameterized in large-scale numerical models (Lott and Miller 1997; Gregory et al. 1998) because the resolution of these models is insufficient to explicitly represent them, as the grid spacing is generally larger than the size of mesoscale mountains. Therefore, investigating the momentum fluxes and gravity wave drag produced by mesoscale mountains is of great relevance for numerical weather and climate prediction (McFarlane 1987; Kim et al. 2003). It is also a topic of importance on its own right from a more fundamental fluid mechanics point of view.

Most studies of the effects of atmospheric gravity waves have focused on two aspects: the surface drag, which defines the total amount of momentum that becomes available to be distributed vertically as the reaction force exerted on the atmosphere; and the variation of the momentum flux with height, which is what has a direct impact on the large-scale flow. The surface drag has been the object of many studies, several of them analytical (Phillips 1984; Smith 1986). The formulas obtained from linear theory for the surface drag in the case of an atmosphere with constant wind and static stability and idealized topography are widely used

Corresponding author address: Miguel A. C. Teixeira, Centro de Geofísica da Universidade de Lisboa, Edifício C8, Campo Grande, 1749-016, Lisbon, Portugal.
E-mail: mateixeira@fc.ul.pt

DOI: 10.1175/2009JAS3065.1

in parameterization schemes (Lott and Miller 1997; Garner 2005). Calculations of how the drag is affected for simple nonconstant wind and stability profiles are also numerous (Smith 1986; Keller 1994; Grubišić and Smolarkiewicz 1997). Recently, Teixeira et al. (2004, hereafter referred to as TMV04) and Teixeira and Miranda (2004, 2006) used a second-order Wentzel–Kramers–Brillouin (WKB) approximation to calculate the drag for generic wind profiles that vary relatively slowly with height. The impact of these effects on the global atmospheric torque was assessed using reanalysis data by Miranda et al. (2009) and found to be as high as 50% on the annual mean in Antarctica. Nonlinear effects on the surface drag have also been addressed since long ago by Miles and Huppert (1969), with the derivation of a correction to the drag using perturbation methods, and by various other authors using numerical simulations (Clark and Peltier 1984; Bacmeister and Pierrehumbert 1988; Miranda and James 1992; Ólafsson and Bougeault 1996).

The variation of momentum flux with height has been the object of only more recent attention, perhaps because parameterization schemes initially employed drag formulas derived for 2D flow (Palmer et al. 1986), and in that case linear theory predicts that all momentum is deposited at isolated, discrete critical levels. However, the interest for flows with directional shear and critical layers (where the wave momentum is deposited over a continuous range of heights, as opposed to critical levels) has increased recently, since these flows are much more realistic. While most parameterization schemes use some form of the saturation criterion derived by Lindzen (1981) to determine the momentum flux profiles (see Kim et al. 2003) the importance of momentum deposition at critical layers (a phenomenon that is within the reach of linear theory) has recently been recognized (Doyle and Jiang 2006). Shutts and Gadian (1999, hereafter referred to as SG99), for example, used linear theory to derive formulas for the momentum flux divergence that corresponds to the drag force acting on the atmosphere, using a WKB approximation. Since they used the standard (first order) WKB approximation, their drag at the surface is not affected by the variation of wind with height, and they assumed that the wave momentum is perfectly absorbed at critical levels. Both of these ideas are consistent with the relatively high Richardson numbers they considered.

The present study presents a model that describes how the momentum flux varies with height at lower Richardson numbers (Ri), for which the surface drag is appreciably affected by wind profile effects and critical layers may not be perfect absorbers. This can be viewed as an extension of the model of TMV04 to the whole atmosphere (i.e., focusing not only on surface quantities), where the WKB approximation is used to obtain momentum flux profiles. As a first step in the development of this theory, the mountains to be considered are assumed to be circular, which is the choice of orography that simplifies the calculations most. It is shown that, in hydrostatic conditions and for generic wind profiles that vary relatively slowly in the vertical, the momentum flux may be expressed as a simple 1D integral that can easily be evaluated numerically, and the momentum flux divergence has a closed analytical form. For high Ri, the obtained expressions tend asymptotically to those derived by SG99.

This paper is organized as follows: in section 2, the theoretical model is described, with an emphasis on the calculation of the momentum flux. In section 3, results are exemplified for two simple idealized wind profiles. Some practical aspects, such as consideration of the finite dimensions of the domain in numerical simulations, are also discussed. Finally, in section 4, the main findings of this study are summarized.

2. Theory

Following TMV04 and Teixeira and Miranda (2006), the inviscid, stationary, nonrotating, hydrostatic equations of motion with the Boussinesq approximation, linearized with respect to a given background state (which depends only on height z) are considered. For a justification of these assumptions, see TMV04. When these equations are differentiated in various ways and combined, it is possible to eliminate all other dependent variables so that a single equation for w, the vertical velocity perturbation, is obtained. Since flow over an isolated mountain is considered, the flow perturbations may be expressed as Fourier integrals along the horizontal directions. The corresponding Fourier transforms are denoted by a hat. The Fourier transform of the vertical velocity perturbation $\hat{w}$ satisfies

$$\hat{w}'' + \left[\frac{N^2(k^2+l^2)}{(Uk+Vl)^2} - \frac{U''k+V''l}{Uk+Vl}\right]\hat{w} = 0, \qquad (1)$$

where N is the Brunt–Väisälä frequency (assumed to be constant) and (U, V) is the basic wind velocity of the incoming flow. This is a hydrostatic version of the Taylor–Goldstein equation (cf. Lin 2007), where (k, l) is the horizontal wavenumber vector and the primes denote differentiation with respect to z.

In the WKB approximation (see, e.g., Bender and Orszag 1999), the vertical coordinate z is rescaled as $Z = \varepsilon z$, where ε is a small dimensionless parameter, so that large variations of z correspond to $O(1)$ variations of Z. In terms of this new vertical coordinate, (1) may be written

$$\varepsilon^2\ddot{\hat{w}} + \left[\frac{N^2(k^2+l^2)}{(Uk+Vl)^2} - \varepsilon^2\frac{\ddot{U}k+\ddot{V}l}{Uk+Vl}\right]\hat{w} = 0, \qquad (2)$$

where differentiation with respect to Z has been replaced by a dot, for simplicity of notation. The solution to (2) is of the form

$$\hat{w} = \hat{w}(Z=0)\exp\left\{i\varepsilon^{-1}\int_0^Z [m_0(\xi) + \varepsilon m_1(\xi) + \varepsilon^2 m_2(\xi) + \varepsilon^3 m_3(\xi) + \cdots]\,d\xi\right\}, \qquad (3)$$

where $i = \sqrt{-1}$, and m_0, m_1, m_2, and m_3 are the zeroth-, first-, second-, and third-order terms of the series expansion of the vertical wavenumber of the internal gravity waves in powers of ε. This expansion was considered up to second order in TMV04 and Teixeira and Miranda (2004, 2006) because that is the only way the variation of the wind with height may have an impact on the surface drag. This procedure yields a surface drag expression that is accurate also to second order. However, the momentum flux in the whole atmosphere accurate to second order is only obtained if the vertical wavenumber is determined up to third order. This is easily shown by Taylor-expanding the terms proportional to powers of ε in the exponent of (3) and is due to the fact that integration lowers by one the order of the various terms contained in this exponent. For the surface drag, this effect is irrelevant, since this drag only depends on quantities where the integral on the exponent of (3) is zero. However, for the calculations presented next, m_3 must be determined.

Inserting (3) into (2), the solutions for m_0, m_1, m_2, and m_3 are easily obtained, yielding

$$m_0 = \frac{N(k^2+l^2)^{1/2}}{Uk+Vl}, \qquad (4)$$

$$m_1 = -\frac{1}{2}i\frac{\dot{U}k+\dot{V}l}{Uk+Vl}, \qquad (5)$$

$$m_2 = -\frac{1}{8}\frac{(\dot{U}k+\dot{V}l)^2}{N(k^2+l^2)^{1/2}(Uk+Vl)} - \frac{1}{4}\frac{(\ddot{U}k+\ddot{V}l)}{N(k^2+l^2)^{1/2}}, \qquad (6)$$

$$m_3 = -\frac{1}{8}i\frac{(Uk+Vl)(\dddot{U}k+\dddot{V}l)}{N^2(k^2+l^2)} - \frac{1}{4}i\frac{(\dot{U}k+\dot{V}l)(\ddot{U}k+\ddot{V}l)}{N^2(k^2+l^2)}. \qquad (7)$$

The boundary conditions to be applied to the solution (3) are the following: The wind must be tangent to the terrain at the surface,

$$\hat{w}(z=0) = i(U_0k + V_0l)\hat{h}, \qquad (8)$$

where $(U_0, V_0) = [U(z=0), V(z=0)]$ is the surface basic wind vector and $\hat{h}$ is the Fourier transform of the terrain elevation. The wave energy must also be radiated upward as $z \to +\infty$. This last condition is incorporated in the definition of m_0, as given by (4), since in that expression m_0 has the same sign as $(Uk + Vl)$, and it can be shown that this corresponds to upward wave energy propagation.

This totally specifies the solution to the problem. To have a closed-form analytical expression for (3), it would be necessary to calculate the integral in the exponent. Although terms m_1 and m_3 may be integrated analytically, for terms m_0 and m_2 this is generally not possible. In TMV04 and Teixeira and Miranda (2006), there was no concern with this integral, because only the surface drag was calculated. This drag only depends on the pressure perturbation at the surface, and that pressure perturbation can be expressed in terms of $\hat{w}$ and $\hat{w}'$ at the surface, where the integral in the exponent reduces to zero, as mentioned above. However, for the purpose of calculating the momentum flux as a function of height, it would seem necessary to determine the wave solutions in the whole domain. Although this is possible for the simple wind profiles considered in TMV04 and Teixeira and Miranda (2006), by a fortunate quirk of the calculations, it is not necessary for obtaining the momentum flux, as will be shown next. The consequence is that the momentum flux may be cast in a fairly simple analytical form for generic wind profiles.

a. The momentum flux

Multiplying the horizontal momentum equations by the vertical streamline displacement η, and noting that $w = U\partial\eta/\partial x + V\partial\eta/\partial y$, it may be shown that

$$D_x = \int_{-\infty}^{+\infty}\int_{-\infty}^{+\infty} p(z=0)\frac{\partial h}{\partial x}\,dx\,dy = -\rho_0\int_{-\infty}^{+\infty}\int_{-\infty}^{+\infty} uw(z=0)\,dx\,dy, \qquad (9)$$

$$D_y = \int_{-\infty}^{+\infty}\int_{-\infty}^{+\infty} p(z=0)\frac{\partial h}{\partial y}\,dx\,dy = -\rho_0\int_{-\infty}^{+\infty}\int_{-\infty}^{+\infty} vw(z=0)\,dx\,dy, \qquad (10)$$

where ρ_0 is a reference density (assumed to be constant), u and v are the horizontal velocity perturbations induced by the orography, p is the pressure perturbation, $\eta(z = 0) = h$ and $h(x, y)$ is the terrain elevation. So the surface drag is numerically equal to the vertical flux of horizontal momentum produced by the mountain at the surface. Additionally, Eliassen–Palm's theorem states that, in the same circumstances, the momentum flux is constant with height except at critical levels (Broad 1995). For a directionally sheared flow and a 3D mountain, there is no single critical level, but a distribution of them with height, depending on the wavenumber of the gravity waves (i.e., a critical layer). This study aims to calculate the momentum flux in such situations of directional shear and 3D orography, addressed first by SG99.

The momentum flux may be calculated in either physical space or Fourier space, based on Parseval's theorem (see Lin 2007, p. 179), as

$$M_i = -\rho_0 \int_{-\infty}^{+\infty}\int_{-\infty}^{+\infty} u_i w \, dx \, dy = -4\pi^2\rho_0 \int_{-\infty}^{+\infty}\int_{-\infty}^{+\infty} \hat{u}_i^* \hat{w} \, dk \, dl \quad (i = 1, 2), \tag{11}$$

where the asterisk denotes complex conjugate, $\hat{u}_1 = \hat{u}$ and $\hat{u}_2 = \hat{v}$ are the Fourier transforms of the horizontal velocity perturbations, respectively, along x and along y, and $M_1 = M_x$, $M_2 = M_y$ are the vertical momentum fluxes in the same directions. We include the minus sign in these definitions so that the momentum fluxes are generally positive, although it should be understood that they are in fact in the downward direction.

To proceed from (11), it should be noted that, from the equations of motion, and from (3), $\hat{u}$ and $\hat{v}$ are related to $\hat{w}$ through

$$\hat{u} = \frac{i}{k^2 + l^2}\left(ikm - l\frac{V'k - U'l}{Uk + Vl}\right)\hat{w}, \tag{12}$$

$$\hat{v} = \frac{i}{k^2 + l^2}\left(ilm + k\frac{V'k - U'l}{Uk + Vl}\right)\hat{w}, \tag{13}$$

where $m = m_0 + \varepsilon m_1 + \varepsilon^2 m_2 + \varepsilon^3 m_3$ is the vertical wavenumber of the internal gravity waves. Using (12) and (13), (11) becomes

$$M_x = 4\pi^2\rho_0 \int_{-\infty}^{+\infty}\int_{-\infty}^{+\infty} \frac{1}{k^2 + l^2}\left(km^* - il\frac{V'k - U'l}{Uk + Vl}\right)|\hat{w}|^2 \, dk \, dl, \tag{14}$$

$$M_y = 4\pi^2\rho_0 \int_{-\infty}^{+\infty}\int_{-\infty}^{+\infty} \frac{1}{k^2 + l^2}\left(lm^* + ik\frac{V'k - U'l}{Uk + Vl}\right)|\hat{w}|^2 \, dk \, dl. \tag{15}$$

Noting, additionally, that the momentum flux is a real quantity, and using (3) again, along with the boundary condition (8), (14) and (15) simplify further to

$$M_i = 4\pi^2\rho_0 \int_{-\infty}^{+\infty}\int_{-\infty}^{+\infty} \frac{k_i}{k^2 + l^2}\mathrm{Re}(m)(U_0 k + V_0 l)^2 |\hat{h}|^2 e^{-2\mathrm{Im}(s)} \, dk \, dl \quad (i = 1, 2), \tag{16}$$

where $k_1 = k, k_2 = l, s = \int_0^z m(\varepsilon\xi)\, d\xi$, Re denotes "real part" and Im denotes "imaginary part."

Hence, to calculate either M_x or M_y as a function of height it is necessary to know both Re(m) and Im(s). Concerning the calculation of Im(s), the facts that m_1 and m_3 may be integrated analytically and that m_0 and m_2 are real [see (4) and (6)] explain why generic wind profiles may be considered: the imaginary part of the integral of the two latter quantities may only come from singularities, as will be shown next.

From (4)–(7), it is straightforward to see that

$$\mathrm{Re}(m) = \frac{N(k^2 + l^2)^{1/2}}{Uk + Vl}\left[1 - \frac{1}{8}\frac{(U'k + V'l)^2}{N^2(k^2 + l^2)} - \frac{1}{4}\frac{(Uk + Vl)(U''k + V''l)}{N^2(k^2 + l^2)}\right], \tag{17}$$

correct to third order in ε. The calculation of Im(s) is somewhat more involved. To simplify this problem, it should be noted first that, like m, s may also be expressed as a power series of ε, $s = s_{-1} + s_0 + s_1 + s_2$, where

$$s_{-1} = \int_0^z m_0(\varepsilon\xi)\, d\xi, \quad s_0 = \varepsilon \int_0^z m_1(\varepsilon\xi)\, d\xi,$$
$$s_1 = \varepsilon^2 \int_0^z m_2(\varepsilon\xi)\, d\xi, \quad s_2 = \varepsilon^3 \int_0^z m_3(\varepsilon\xi)\, d\xi. \quad (18)$$

Each of these terms will be considered separately.

Since m_0 is a real quantity, its integral, given by s_{-1}, may only have an imaginary part due to singularities. Assuming that m_0 decays to zero sufficiently fast toward infinity in the complex plane, the singularities may only occur at the points where the denominator of m_0 is zero, namely critical levels. So, below any critical levels (i.e., for $z < z_c$), $\mathrm{Im}(s_{-1}) = 0$. Above critical levels, the following contour integral should be considered:

$$\oint_C m_0\, d\xi = \int_{C_1} m_0\, d\xi + \int_{C_2} m_0\, d\xi + \int_{C_3} m_0\, d\xi + \int_{C_4} m_0\, d\xi$$
$$= 2\pi i\, \mathrm{Res}(m_0, z_c), \quad (19)$$

where the closed contour in the complex plane C is split into four segments, C_1, C_2, C_3, and C_4, represented in Fig. 1. In (19), the integral is equaled to the residue of m_0 at z_c, because that is the only singularity inside the integration path. This means that

$$\mathrm{Im}\left(\int_{C_1} m_0\, d\xi + \int_{C_3} m_0\, d\xi\right)$$
$$= \mathrm{Im}\left[2\pi i\, \mathrm{Res}(m_0, z_c) - \int_{C_2} m_0\, d\xi - \int_{C_4} m_0\, d\xi\right]. \quad (20)$$

When the radius of the inner semicircle $C_2(\delta)$ approaches zero, and the radius of the outer semicircle $C_4(R)$ approaches infinity, the expression on the left-hand side of (20) tends to $\mathrm{Im}(s_{-1})$, because the parts of the integral along the real axis for $\xi < 0$ or $\xi > z$ have no imaginary part. On the other hand the integral along C_4 on the right-hand side tends to zero. Therefore, it can be concluded that

$$\mathrm{Im}(s_{-1}) = \mathrm{Im}\left[2\pi i\, \mathrm{Res}(m_0, z_c) - \int_{C_2} m_0\, d\xi\right]$$
$$= \mathrm{Im}\left[\int_0^{\pi} \frac{N(k^2 + l^2)^{1/2}}{(U_c' k + V_c' l)\delta e^{i\vartheta}} i\delta e^{i\vartheta}\, d\vartheta\right], \quad (21)$$

where polar coordinates (in the complex plane) have been adopted in the second equality, $Uk + Vl$ has been expanded in a Taylor series around the critical level, and (U_c', V_c') are the vertical derivatives of the background wind at the critical level. Equation (21) is valid when $U_c' k, V_c' l > 0$ because it can be shown that in this case the singularity, with the addition of a Rayleigh damping to the equations of motion, moves to the positive imaginary semiplane (cf. Booker and Bretherton 1967; Grubišić and Smolarkiewicz 1997). When $U_c' k, V_c' l < 0$, on the other hand, this singularity moves to the negative imaginary semiplane, and it is necessary to use an integration contour that is the mirror image with respect to the real axis of that shown in Fig. 1. This gives a symmetric final result. This calculation therefore yields

$$\mathrm{Im}(s_{-1}) = 0 \quad \text{if} \quad z < z_c,$$
$$\mathrm{Im}(s_{-1}) = \pi \frac{N(k^2 + l^2)^{1/2}}{|U_c' k + V_c' l|} \quad \text{if} \quad z > z_c. \quad (22)$$

s_0 may be obtained by direct integration, and the result is the following:

$$\mathrm{Im}(s_0) = -\frac{1}{2} \log\left|\frac{Uk + Vl}{U_0 k + V_0 l}\right|. \quad (23)$$

For the calculation of s_1, the same procedure must be followed as for s_{-1}. It turns out that the terms involving the second derivatives of the wind profile in m_2 can be integrated directly, and are purely real, so they do not

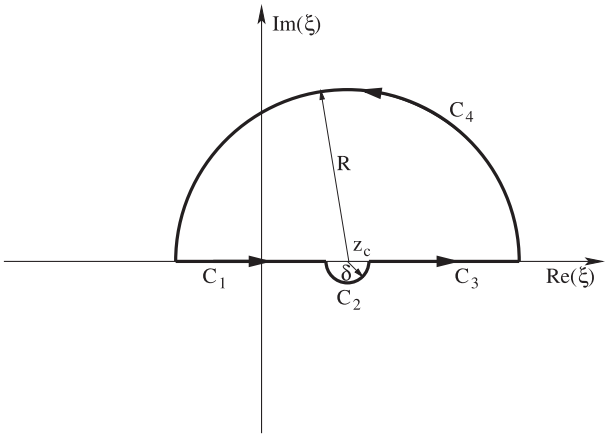

FIG. 1. Schematic diagram of the integration path used for calculating the integrals of the vertical wavenumber. The various segments of this path are C_1, C_2, C_3, and C_4; δ is the radius of the inner semicircle and R is the radius of the outer semicircle. The complex coordinate is ξ and the height of the critical level (on the real axis) is z_c.

contribute to $\mathrm{Im}(s_1)$. Therefore, this quantity only receives a contribution from the critical level and is found to be

$$\mathrm{Im}(s_1) = 0 \quad \text{if} \quad z < z_c,$$
$$\mathrm{Im}(s_1) = -\frac{\pi}{8}\frac{|U_c'k + V_c'l|}{N(k^2+l^2)^{1/2}} \quad \text{if} \quad z > z_c. \tag{24}$$

Finally, s_2 may also be obtained by direct integration, yielding

$$\mathrm{Im}(s_2) = \frac{1}{16}\frac{(U_0'k + V_0'l)^2}{N^2(k^2+l^2)} + \frac{1}{8}\frac{(U_0k + V_0l)(U_0''k + V_0''l)}{N^2(k^2+l^2)} - \frac{1}{16}\frac{(U'k + V'l)^2}{N^2(k^2+l^2)} - \frac{1}{8}\frac{(Uk + Vl)(U''k + V''l)}{N^2(k^2+l^2)}. \tag{25}$$

Adding all the three terms, one obtains

$$\mathrm{Im}(s) = \mathrm{Im}(s_0) + \mathrm{Im}(s_2) \quad \text{if} \quad z < z_c,$$
$$\mathrm{Im}(s) = \mathrm{Im}(s_0) + \mathrm{Im}(s_2) + \pi\frac{N(k^2+l^2)^{1/2}}{|U_c'k + V_c'l|}\left[1 - \frac{1}{8}\frac{(U_c'k + V_c'l)^2}{N^2(k^2+l^2)}\right] \quad \text{if} \quad z > z_c. \tag{26}$$

Inserting the definitions of $\mathrm{Re}(m)$ and $\mathrm{Im}(s)$ given by (17) and (26) into (16) yields

$$M_i = 4\pi^2\rho_0 N\int_{-\infty}^{+\infty}\int_{-\infty}^{+\infty}|\hat{h}|^2\frac{k_i}{(k^2+l^2)^{1/2}}|U_0k + V_0l|\,\mathrm{sgn}(Uk + Vl)[1 - S(k,l,z)] \times \exp[S(k,l,z) - S(k,l,z=0)]\exp[-2\pi H(z - z_c)C(k,l)]\,dk\,dl, \tag{27}$$

for $i = 1, 2$, where

$$S = \frac{1}{8}\frac{(U'k + V'l)^2}{N^2(k^2+l^2)} + \frac{1}{4}\frac{(Uk + Vl)(U''k + V''l)}{N^2(k^2+l^2)}, \tag{28}$$

$$C = \frac{N(k^2+l^2)^{1/2}}{|U_c'k + V_c'l|}\left[1 - \frac{1}{8}\frac{(U_c'k + V_c'l)^2}{N^2(k^2+l^2)}\right], \tag{29}$$

and where $H(z)$ denotes the Heaviside step function. Now, the critical level z_c inside the argument of this function, and consequently also (U_c', and V_c'), are in fact in general functions of the wavenumber for directionally sheared flows. So an alternative way to express the transition of the wave solutions at the critical level is by defining appropriately the limits of integration in the integrals of (27), as will be done next (cf. SG99). This is especially simple using polar coordinates for representing the horizontal wavenumber vector,

$$k = \kappa\cos\theta, \quad l = \kappa\sin\theta, \tag{30}$$

where $\kappa = (k^2 + l^2)^{1/2}$ is the magnitude of the wavenumber. It is also convenient to express the incoming wind velocity in polar coordinates:

$$U = \mathcal{U}\cos\psi, \quad V = \mathcal{U}\sin\psi, \tag{31}$$

where $\mathcal{U}$ is the wind speed and ψ is the wind direction. In this case, the condition defining critical levels is simply $\cos(\theta - \psi) = 0$, implying that the wavenumber and the wind direction must be perpendicular, as is well known (Teixeira et al. 2008, hereafter TMA08).

It should be recalled at this point that the mountain that generates the internal gravity waves is assumed to be circular. This is done for illustrative purposes, since a circular mountain forces internal gravity waves possessing horizontal wavenumbers with all azimuthal angles. This is useful for understanding how critical levels affect the different wavenumbers. Additionally, using a circular mountain enables further simplification of (27), when expressed in polar coordinates, because in that case $\hat{h}(k,l) = \hat{h}(\kappa)$ and the integrals in κ and θ may be separated. Equation (27) thus becomes

$$M_x = 4\pi^2\rho_0 N\int_0^{+\infty}\kappa^2|\hat{h}|^2\,d\kappa\int_0^{2\pi}\cos\theta|U_0\cos\theta + V_0\sin\theta|\,\mathrm{sign}(U\cos\theta + V\sin\theta) \times [1 - S(\theta,z)]\exp[S(\theta,z) - S(\theta,z=0)]\exp[-2\pi H(z - z_c)C(\theta)]\,d\theta, \tag{32}$$

for M_x, where

$$S = \frac{1}{8}\frac{(U'\cos\theta + V'\sin\theta)^2}{N^2} + \frac{1}{4}\frac{(U\cos\theta + V\sin\theta)(U''\cos\theta + V''\sin\theta)}{N^2}, \quad (33)$$

$$C = \frac{N}{|U_c'\cos\theta + V_c'\sin\theta|}\left[1 - \frac{1}{8}\frac{(U_c'\cos\theta + V_c'\sin\theta)^2}{N^2}\right]. \quad (34)$$

Note how, in the hydrostatic approximation, S and C are only functions of θ (apart from z). The only difference for M_y is that the factor $\cos\theta$ in the integrand of the second integral in (32) is replaced by $\sin\theta$.

Noting that the surface drag in the absence of shear for a generic type of circular mountain is given by $D_0 = 4\pi^3\rho_0 N\mathcal{U}_0\int_0^\infty \kappa^2|\hat{h}|^2\,dk$, where $\mathcal{U}_0 = \mathcal{U}(z=0)$, M_x may be normalized by this value, as $\tilde{M}_x = M_x/D_0$, yielding

$$\tilde{M}_x = \frac{1}{\pi}\int_0^{2\pi} \cos\theta\left|\cos(\theta-\psi_0)\right|\operatorname{sgn}[\cos(\theta-\psi)][1-S(\theta,z)] \times \exp[S(\theta,z) - S(\theta,z=0)] \times \exp[-2\pi H(z-z_c)C(\theta)]\,d\theta, \quad (35)$$

where $\psi_0 = \psi(z=0)$. This shows that $\tilde{M}_x$ is independent of the form of $\hat{h}$ [or $h(x,y)$] for any circular mountain, as happened for the normalized surface drag in TMV04 and TMA08.

It will be assumed additionally that the wind profile, while having directional shear, only has one critical level for each wavenumber; that is, the wind direction has a monotonic variation with height and does not turn by an angle larger than π. In that case, the wind, from the surface to a generic level z, spans a certain range of wind direction angles from ψ_0 to $\psi(z)$. To this range of angles correspond two ranges of wavenumbers for waves that have been ''filtered'' (not necessarily totally absorbed) by the critical levels (see discussion in TMA08). These filtered wavenumbers or, more exactly, wavenumber directions, are represented as the horizontally hatched regions in Fig. 2. Taking into account that, due to the Heaviside function, the exponential in (35) only differs from one for wavenumbers that have been filtered, $\tilde{M}_x$ may also be expressed as

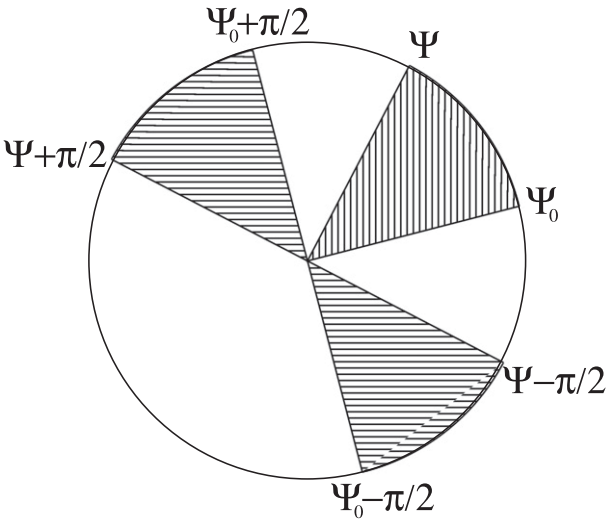

FIG. 2. Schematic diagram illustrating the angular interval spanned by a wind profile that rotates counterclockwise with height (vertical hatching), where ψ_0 is the wind angle at the surface and ψ is the wind angle at the (generic) height under consideration (z). The ranges of angles of horizontal wavenumbers that have critical levels between the surface and z are denoted by the horizontal hatching.

$$\tilde{M}_x = \frac{1}{\pi}\left(\int_{\psi-\pi/2}^{\psi_0+\pi/2} I_1\,d\theta + \int_{\psi+\pi/2}^{\psi_0+3\pi/2} I_1\,d\theta - \int_{\psi_0+\pi/2}^{\psi+\pi/2} I_1 I_2\,d\theta - \int_{\psi_0+3\pi/2}^{\psi+3\pi/2} I_1 I_2\,d\theta\right), \quad (36)$$

where

$$I_1 = \cos\theta\cos(\theta-\psi_0)[1-S(\theta,z)] \times \exp[S(\theta,z) - S(\theta,z=0)], \quad (37)$$

$$I_2 = \exp[-2\pi C(\theta)], \quad (38)$$

for a wind that turns counterclockwise with height. For a wind that turns clockwise, ψ_0 and ψ must be exchanged in (36).

It turns out that the first and second integral and the third and fourth integral in (36) are equal by symmetry, so finally $\tilde{M}_x$ is given by

$$\tilde{M}_x = \frac{2}{\pi}\left(\int_{\psi-\pi/2}^{\psi_0+\pi/2} I_1\,d\theta - \int_{\psi_0+\pi/2}^{\psi+\pi/2} I_1 I_2\,d\theta\right) \quad (39)$$

for a counterclockwise–turning wind. Defining

$$I_3 = \sin\theta\cos(\theta-\psi_0)[1-S(\theta,z)] \times \exp[S(\theta,z) - S(\theta,z=0)], \quad (40)$$

it is possible to express the momentum flux along y in a formally similar way:

$$\tilde{M}_y = \frac{2}{\pi}\left(\int_{\psi-\pi/2}^{\psi_0+\pi/2} I_3\, d\theta - \int_{\psi_0+\pi/2}^{\psi+\pi/2} I_3 I_2\, d\theta\right), \qquad (41)$$

where M_y has also been normalized by the surface drag in the absence of shear D_0 (and is also independent of the form of $\hat{h}$).

b. The momentum flux divergence

What is directly relevant to the parameterization of gravity wave drag in numerical models is the divergence of the momentum fluxes. Integrated over the area surrounding the mountain, this divergence is simply the vertical derivative of the $\tilde{M}_x$ and $\tilde{M}_y$ determined above. If this calculation is performed, the following expressions are obtained, correct to second order in ε:

$$\frac{d\tilde{M}_x}{dz} = -\frac{2}{\pi}\psi' \sin\psi \sin(\psi-\psi_0)[1-S_\psi(z)] \times \exp[S_\psi(z) - S_\psi(z=0)] \times\{1 + \exp[-2\pi C_\psi(z)]\}, \qquad (42)$$

$$\frac{d\tilde{M}_y}{dz} = \frac{2}{\pi}\psi' \cos\psi \sin(\psi-\psi_0)[1-S_\psi(z)] \times \exp[S_\psi(z) - S_\psi(z=0)] \times \{1 + \exp[-2\pi C_\psi(z)]\}, \qquad (43)$$

where

$$S_\psi(z) = \frac{1}{8}\frac{(U'\sin\psi - V'\cos\psi)^2}{N^2} + \frac{1}{4}\frac{(U\sin\psi - V\cos\psi)(U''\sin\psi - V''\cos\psi)}{N^2}, \qquad (44)$$

$$C_\psi(z) = \frac{N}{|U_c'\sin\psi - V_c'\cos\psi|}\left[1 - \frac{1}{8}\frac{(U_c'\sin\psi - V_c'\cos\psi)^2}{N^2}\right], \qquad (45)$$

and U_c', V_c' are evaluated at the azimuthal angle ψ. Note how (42) and (43) are in closed analytical form. It can also be easily verified that these expressions satisfy the equivalent to Eliassen–Palm's theorem in three dimensions (Broad 1995):

$$U\frac{dM_x}{dz} + V\frac{dM_y}{dz} = 0. \qquad (46)$$

Finally, if the shear is weak, $S_\psi \to 0$, and $C_\psi \to +\infty$, and it can be shown that (42) and (43) asymptotically tend to expressions equivalent to Eqs. (22) and (23) of SG99, with the appropriate normalization.

3. Results

The preceding formulas for the momentum flux will be applied next to simple idealized wind profiles. The simplest profiles with directional shear are those where one or both of the wind components vary linearly with height, or where the wind turns with height at a constant rate maintaining its magnitude. Two of these profiles, which have the simplifying property of having a constant Richardson number, will be considered next (cf. TMV04; Teixeira and Miranda 2006). In fact, linear wind profiles do not strictly satisfy one of the assumptions used in deriving (39) and (41), namely that the integral of m along C_4 tends to zero as the radius of this semicircle R tends to infinity. However, the log function that arises in this case (which can be handled analytically) has a branch line along the negative real axis (see TMA08). This branch line has a compensating effect on the solutions, and it may be shown that (39) and (41) can be used in this case as if the violated assumption was satisfied. This was checked by computing the solutions for this type of wind profile directly (as was done in TMA08, i.e., without using the residue theorem arguments outlined above) and noting that the results were the same. A wind profile where the wind turns with height maintaining its magnitude (or other profile where the wind speed is bounded) does not have this problem, as it satisfies the above-mentioned assumption from the outset.

a. Practical aspects

A comparison of the results of the analytical model presented above with numerical simulations entails consideration of some practical aspects.

First, the analytical model uses the Boussinseq approximation, while numerical models do not. A leading-order treatment of non-Boussinesq effects can be achieved, as is well known (e.g., Smith 1979; SG99) through multiplication of the velocity perturbations by a factor $(\rho_0/\rho)^{1/2}$, where $\rho(z)$ is a depth-dependent density. For the momentum fluxes, this effect is irrelevant, since the momentum fluxes computed numerically include the

density, whose decay therefore cancels with the amplifying factors affecting the velocity perturbations.

A second effect that must be accounted for is the limited horizontal extent of the computational domain in numerical simulations. As noted by SG99 and before by Leutbecher (1998), the wave field generated by an isolated mountain tends to widen and propagate laterally outside the domain as height increases. This is one of the possible processes leading to a decay of the momentum fluxes with height in addition to the effect of critical levels. Although, as will be seen, for relatively low Ri, wave filtering by critical levels should be considerably more dominant than in the numerical simulations of SG99; the effect of the finite dimensions of the domain should be evaluated here. For that purpose, apart from using the previously derived expressions for the momentum flux profiles, we also calculate the momentum fluxes in a domain of finite horizontal extent, equal to that used in the numerical simulations. This is done using the expressions

$$M_x = -\rho_0 \int_{-L_x/2}^{+L_x/2} \int_{-L_y/2}^{+L_y/2} uw \, dx \, dy,$$
$$M_y = -\rho_0 \int_{-L_x/2}^{+L_x/2} \int_{-L_y/2}^{+L_y/2} vw \, dx \, dy, \qquad (47)$$

where L_x and L_y are the dimensions of the domain along x and y. In (47), the integrals are calculated numerically and u, v, and w are evaluated using the analytical expressions for $\hat{u}$, $\hat{v}$, and $\hat{w}$ obtained from linear theory with the WKB approximation. This implies calculating not only the imaginary part of s (as before) but also its real part, which can be done analytically for both wind profiles considered next, but not in general.

b. Numerical simulations

The numerical simulations carried out use the NH3D nonlinear and nonhydrostatic numerical model, which is described in Miranda and James (1992). This model uses a pressure-based terrain-following sigma vertical coordinate. For all simulations, the model is run for a grid of 121×121 points in the horizontal directions, with grid spacing of 3 km, by 200 levels in the vertical. For the simulations with a linear wind profile, the top of the domain is at 50 mb and the vertical resolution varies between 40 m (at the surface) and 400 m (at the top of the computational domain). For the simulations considering a turning wind with Ri = 0.5 or 1, the top of the domain is at 300 mb and the vertical resolution varies between 29 and 75 m. For Ri = 5, the top of the domain is raised to 100 mb. Cosine-squared-type sponges are applied laterally at the 10 outer points of the domain, and also at the top of the domain, above $z = 10$ km, for the linear wind profile. It is unnecessary to use a sponge at the top of the domain in the turning wind case.

The model is run in inviscid and nonrotating mode. A Brunt–Väisälä frequency of $N = 0.01\ \mathrm{s}^{-1}$ and a wind speed at the surface of $|\mathbf{U}_0| = 7.07\ \mathrm{m\ s}^{-1}$ are considered in all simulations. The circular mountain that forces the internal gravity waves is a bell-shaped mountain, with the form

$$h(x, y) = \frac{h_0}{[1 + (x/a)^2 + (y/a)^2]^{3/2}}. \qquad (48)$$

The mountain half-width is assumed to be $a = 14.14$ km and the mountain height takes the following values: $h_0 =$ 7.07, 70.7, 141.4, 353.5 m. This implies that the dimensionless mountain width is $Na/|\mathbf{U}_0| = 20$ in all runs, meaning that the flow is nearly hydrostatic. Additionally, the dimensionless mountain height is $Nh_0/|\mathbf{U}_0| =$ 0.01, 0.1, 0.2, 0.5, that is, highly linear to weakly nonlinear conditions. The simulations are carried out over a number of 20 000 time steps of 6 s (approximately 33 h), until the momentum flux stabilizes.

The momentum fluxes obtained in the numerical simulations are integrated over the 101×101 inner grid points of the domain, avoiding the lateral sponges, where the flow field is unreliable. The domain limits used in the limited-area WKB results given by (47) are consistent with this procedure, being $L_x = L_y = 300$ km.

c. Linear wind profile

The analytical expressions obtained in previous sections show that the impact of wind profile variations on the momentum flux is purely local. This result only holds for wind profiles that vary sufficiently slowly. It was shown by TMA08 that the surface drag (and so necessarily also the momentum flux) may be strongly influenced by shear discontinuities existing aloft, due to wave energy reflection, especially at low Ri, unless a large fraction of the wave spectrum has critical levels beneath those discontinuities. For that reason, wind profiles such as the linear profile used by Shutts (1995) or SG99 are not very appropriate for testing the present model, since the wind turns at most by $\pi/2$, so the waves are very incompletely filtered by critical levels. Realistic wind profiles that can be approximated by this idealized profile near the surface must have their magnitude limited aloft by some sudden or less sudden variation of the shear rate, so it is likely that the corresponding momentum fluxes differ appreciably from those calculated assuming that the constant shear extends indefinitely.

A linear wind profile more appropriate for the present purposes, where the wind direction spans approximately

one and a half quadrants, and so where there is more complete momentum deposition at critical levels, is

$$U = U_0 - \alpha z, \quad V = U_0, \tag{49}$$

where $U_0 > 0$ and $\alpha > 0$ are constants. This was one of the wind profiles employed by TMV04 and TMA08. TMA08, in particular, showed how the value of the surface drag in this case was relatively insensitive to shear discontinuities existing aloft.

For an infinite horizontal domain, the momentum flux is given theoretically for this wind profile by (39) and (41), but since $V' = U'' = V'' = 0$ and $U' = -\alpha$, I_1, I_2, and I_3 simplify to

$$I_1 = \cos\theta \cos\left(\theta - \frac{\pi}{4}\right)\left(1 - \frac{1}{8\mathrm{Ri}} \cos^2\theta\right), \tag{50}$$

$$I_2 = \exp\left[-2\pi \frac{\mathrm{Ri}^{1/2}}{|\cos\theta|}\left(1 - \frac{1}{8\mathrm{Ri}} \cos^2\theta\right)\right], \tag{51}$$

$$I_3 = \sin\theta \cos\left(\theta - \frac{\pi}{4}\right)\left(1 - \frac{1}{8\mathrm{Ri}} \cos^2\theta\right), \tag{52}$$

where $\mathrm{Ri} = N^2/\alpha^2$ is the Richardson number of the incoming flow. On the other hand, the momentum flux divergence is given theoretically by (42) and (43), but with

$$S_\psi(z) = \frac{1}{8\mathrm{Ri}} \sin^2\psi, \quad C_\psi(z) = \frac{\mathrm{Ri}^{1/2}}{|\sin\psi|}\left(1 - \frac{1}{8\mathrm{Ri}} \sin^2\psi\right). \tag{53}$$

Figure 3 shows M_x and M_y as a function of dimensionless height $\alpha z/|\mathbf{U}_0|$ for Ri = 0.5, 1, and 5 (Figs. 3a,b; 3c,d; and 3e,f, respectively) and for $Nh_0/|\mathbf{U}_0| = 0.01$, 0.1, 0.2, 0.5 (in each panel), normalized by the corresponding drag components in the absence of shear. This alternative normalization, which will only be used for the present wind profile, amounts to multiplying $\tilde{M}_x$ and $\tilde{M}_y$, as defined previously, by $\sqrt{2}$, and the aim is to make both components of the momentum flux tend to 1 when $\mathrm{Ri} \to +\infty$.

Admittedly, Ri = 0.5, the lowest Ri considered, is rather low for the approach employed here. However, previous studies by TMV04 and Teixeira and Miranda (2004, 2006) have shown that at this value of Ri the WKB approximation is still surprisingly accurate. Additionally, although deep atmospheric layers with low Ri are seldom found in nature, the aim here is to test the limits of the present model and to show its differences from that of SG99. Finally, it should be emphasized that the present model may be applied to any wind profiles that vary sufficiently slowly in the vertical, so this and other ensuing results merely serve to illustrate is behavior.

In Fig. 3, the solid lines correspond to the present WKB model, and the dotted lines to the momentum flux expressions of SG99, which are valid as $\mathrm{Ri} \to +\infty$, both for an infinite horizontal domain. The dashed lines correspond to the WKB model, but for a domain of limited extent (these results will henceforth be called "limited-area WKB model"). The circles, squares, triangles, and diamonds correspond to numerical simulations using the NH3D nonlinear and nonhydrostatic model, respectively, for $Nh_0/|\mathbf{U}_0| = 0.01$, 0.1, 0.2, 0.5. The upper limit $Nh_0/|\mathbf{U}_0| = 0.5$ aims to avoid the possibility of wave breaking and the associated undesirable unsteadiness of the flow.

It can be seen that, for all Ri, the numerical results for $Nh_0/|\mathbf{U}_0| = 0.01$ are closest to the limited-area WKB model. This shows that consideration of the limited domain extent is an important aspect. However, both $\tilde{M}_x$ and $\tilde{M}_y$ are slightly lower in the numerical simulations than in the WKB results, even taking the finite extent of the domain into account, especially at larger heights (and especially for $\tilde{M}_y$). This discrepancy is probably due to additional momentum flux absorption by spurious numerical dissipation. This idea is supported by the behavior of the surface drag in simulations using the same numerical model in Teixeira et al. (2005), or in TMA08. Another interesting aspect is that, as Ri increases, while the difference between the WKB results and the theory of SG99 obviously decreases, the effect of the finite extent of the domain becomes more apparent. That can be attributed to the normalization of the horizontal axis, where the same dimensionless height corresponds to a larger dimensional height at higher Ri. As a consequence, in the latter cases, a greater fraction of the wave perturbation is able to escape the computational domain, as the wave pattern widens upward. It is also curious to note some spurious jumps in the numerical results at the lowest level (see Figs. 3a,c), perhaps due to interpolation problems (the values of u, v, and w are interpolated from sigma model levels to z-constant levels).

As $Nh_0/|\mathbf{U}_0|$ increases, the lower limit for height in the numerical simulation data increases, as can be seen in Fig. 3, because the lowest data point corresponds to the height of the mountain top. But, in terms of the dimensionless height, this effect becomes less pronounced as Ri increases, again because of the normalization used for the horizontal axis. The momentum fluxes are amplified progressively as $Nh_0/|\mathbf{U}_0|$ increases, due to nonlinear effects. For the present wind profile, the y component of the momentum flux is amplified considerably more, and the x component is even smaller than in linear conditions for Ri = 0.5. This is probably related to the fact that this component of the momentum flux

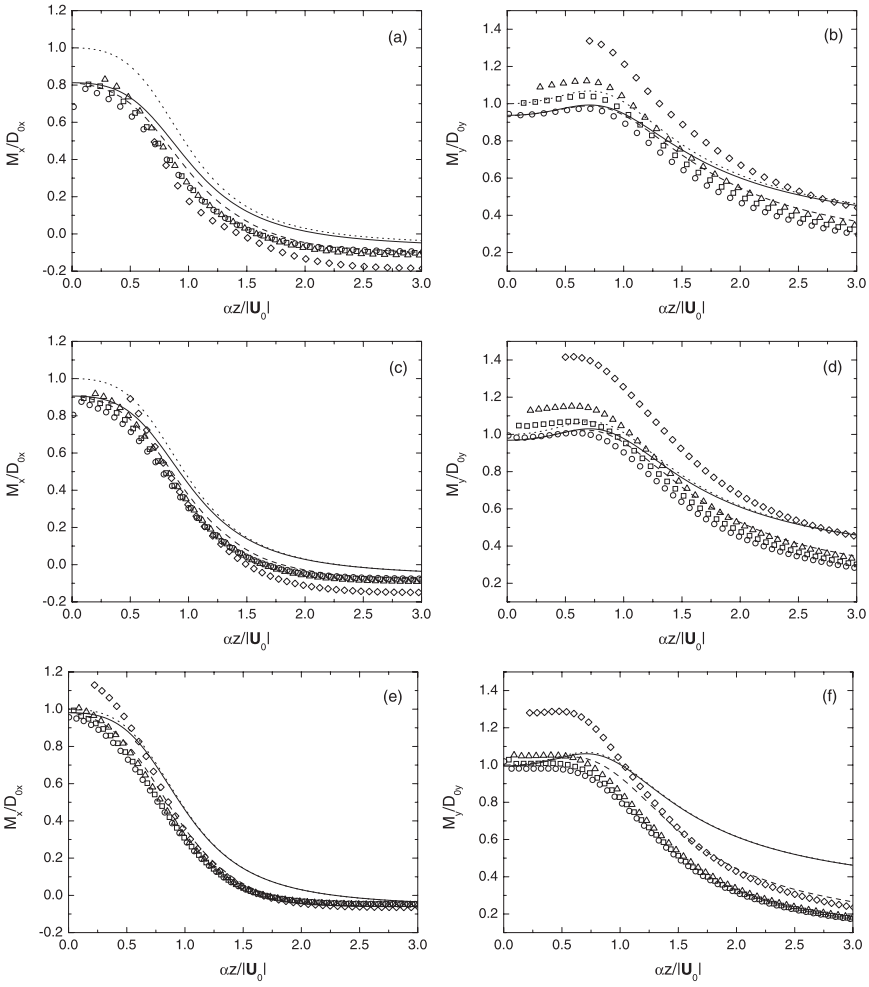

FIG. 3. Normalized momentum fluxes as a function of the normalized height for the linear wind profile (49). Solid lines: WKB model; dotted lines: model of SG99; dashed lines: limited-area WKB model; symbols: numerical results. Circles: $Nh_0/|\mathbf{U}_0| = 0.01$; squares: $Nh_0/|\mathbf{U}_0| = 0.1$; triangles: $Nh_0/|\mathbf{U}_0| = 0.2$; diamonds: $Nh_0/|\mathbf{U}_0| = 0.5$. (a),(b) Ri = 0.5; (c),(d) Ri = 1; (e),(f) Ri = 5; (a),(c),(e) x components; (b),(d),(f) y components.

becomes negative as height increases, due to the turning of the mean wind. The momentum fluxes for $Nh_0/|\mathbf{U}_0| = 0.1$ are still relatively close to those for $Nh_0/|\mathbf{U}_0| = 0.01$ (and to the WKB results), but at $Nh_0/|\mathbf{U}_0| = 0.2$ they start to differ more, and at $Nh_0/|\mathbf{U}_0| = 0.5$ the difference is substantial, as a comparison between Figs. 3b,d,f shows. Nonlinear effects seem to become stronger the lower Ri is, although for example $\tilde{M}_x$ is more amplified near the surface for Ri = 5 than for Ri = 0.5 or Ri = 1. But this may be simply due to the fact that the values of $\tilde{M}_x$ are not displayed at the lowest heights, since these would be below the mountaintop. Figure 3 shows that the effects of nonlinearity at, for example, $Nh_0/|\mathbf{U}_0| = 0.2$ are clearly comparable to the effects of wind profile shear at Ri = 1 or Ri = 0.5. This highlights the practical importance of the present calculations.

d. Wind that turns with height

As a second example, a wind that turns with height at a constant rate maintaining its magnitude is considered (cf. SG99; TMV04). In this case, the wind turns indefinitely, so it spans the two quadrants required for the wave momentum to be totally absorbed at critical levels when Ri is large. The wind components are

$$U = U_0 \cos(\beta z), \quad V = U_0 \sin(\beta z), \tag{54}$$

where $U_0 > 0$ and $\beta > 0$ are constants. In this case, curvature of the wind profile exists, so the expressions of the coefficients in (39) and (41) are slightly more complicated:

$$I_1 = \cos^2\theta\left\{1 + \frac{1}{8\mathrm{Ri}}[2\cos^2(\theta - \beta z) - \sin^2(\theta - \beta z)]\right\} \times \exp\left\{\frac{1}{8\mathrm{Ri}}[\sin^2(\theta - \beta z) - 2\cos^2(\theta - \beta z) - \sin^2\theta + 2\cos^2\theta]\right\}, \quad (55)$$

$$I_2 = \exp\left[-2\pi\mathrm{Ri}^{1/2}\left(1 - \frac{1}{8\mathrm{Ri}}\right)\right], \quad (56)$$

$$I_3 = \sin\theta\cos\theta\left\{1 + \frac{1}{8\mathrm{Ri}}[2\cos^2(\theta - \beta z) - \sin^2(\theta - \beta z)]\right\} \times \exp\left\{\frac{1}{8\mathrm{Ri}}[\sin^2(\theta - \beta z) - 2\cos^2(\theta - \beta z) - \sin^2\theta + 2\cos^2\theta]\right\}, \quad (57)$$

and the coefficients in (42) and (43) are

$$S_\psi(z) = \frac{1}{8\mathrm{Ri}}, \quad C_\psi(z) = \mathrm{Ri}^{1/2}\left(1 - \frac{1}{8\mathrm{Ri}}\right), \quad (58)$$

where $\mathrm{Ri} = N^2/(U_0\beta)^2$ is the Richardson number.

Figure 4 displays the variation of $\tilde{M}_x$ and $\tilde{M}_y$ with dimensionless height $\beta z/\pi$ for the same values of Ri and $Nh_0/|\mathbf{U}_0|$ as shown in Fig. 3. Symbols also have the same meaning as in Fig. 3. This case is qualitatively different in that the drag at the surface is enhanced instead of reduced (see TMV04; Teixeira and Miranda 2006). In the numerical runs for $Nh_0/|\mathbf{U}_0| = 0.01$, $\tilde{M}_x$ shows good agreement with the limited-area WKB model, and also with the WKB model for an infinite domain for Ri = 0.5 and Ri = 1 (which differs little from it). Both WKB models underestimate the numerical results near the surface. A similar underestimation was detected in the surface drag, for example, in Fig. 7 of TMV04, being apparently inherent to the WKB approach. Also inherent to this approach is the large underestimation of the y component of the surface drag (which is incorrectly predicted to be zero) and the consequent underestimation of $\tilde{M}_y$ elsewhere, particularly at low Ri (see Fig. 4b). However, the performance of the WKB models is especially good for $\tilde{M}_x$ at midlevels. The slope of the $\tilde{M}_x$ curve is particularly well captured, for all values of Ri, which means that the momentum flux divergence along x is accurately diagnosed. Additionally, at the top of the displayed region, where the whole wave spectrum has been filtered by critical levels, $\tilde{M}_x$ is also quite accurately predicted, as will be seen in more detail. In this region, $\tilde{M}_x$ has changed its sign, which corresponds to waves that have been attenuated and had their phase shifted by the critical levels (cf. TMA08).

As $Nh_0/|\mathbf{U}_0|$ increases, the magnitudes of both $\tilde{M}_x$ and $\tilde{M}_y$ become considerably larger. This enhancement is somewhat more pronounced than for the linear wind profile, and acts more equally in the two components. In particular, $\tilde{M}_y$ is much larger in the numerical simulations than in any theoretical model, especially at Ri = 0.5 (this is partly enhanced visually by the different scaling of the vertical axis in the graphs of Figs. 4b,d,f). However, for $\tilde{M}_x$ the agreement between numerical and theoretical results is more acceptable, especially for $Nh_0/|\mathbf{U}_0| = 0.1$ and 0.2. Although the $\tilde{M}_x$ given by the theoretical models underestimates both the values and the slope of the curve of the same quantity given by the numerical simulations for $Nh_0/|\mathbf{U}_0| = 0.5$, it is clear that the present WKB calculations provide a substantial improvement over the original model of SG99. This is especially visible at midlevels (e.g., in Fig. 4a), where the model of SG99 underestimates much more severely the momentum flux divergence. Once again, it can be seen that the effects of shear on the momentum flux, at least for $\tilde{M}_x$, have an impact comparable with nonlinear effects at $Nh_0/|\mathbf{U}_0| = 0.2$.

The values of the surface drag given by the present model have been extensively tested in TMV04 and Teixeira and Miranda (2004, 2006). The new decisive aspect presented in this study is the way in which the momentum flux is filtered by critical levels. A stringent test of this aspect is provided by the value of the momentum flux at a height where all wavenumbers in the mountain wave spectrum have passed through their critical levels. The x component of this momentum flux, which for the present wind profile is obtained at a height $\beta z/\pi = 1$, is presented in Fig. 5 as a function of Ri. The solid line corresponds to the present model for an unlimited domain, for which it can be shown that

$$\tilde{M}_x\left(\frac{\beta z}{\pi} = 1\right) = -\left(1 + \frac{5}{32\mathrm{Ri}}\right)\exp\left[-2\pi\mathrm{Ri}^{1/2}\left(1 - \frac{1}{8\mathrm{Ri}}\right)\right]. \quad (59)$$

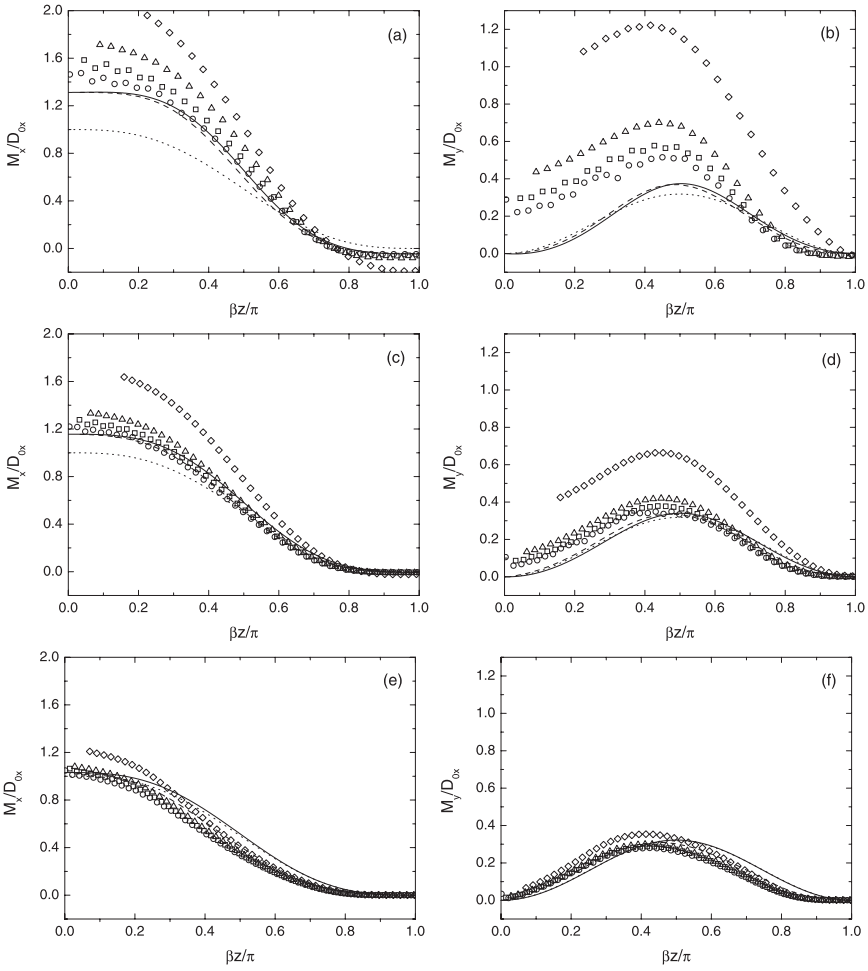

FIG. 4. Same as in Fig. 3, but for a wind that turns with height maintaining its magnitude (54). Note that, unlike Fig. 3, here the vertical axes in (b),(d),(f) have a different scaling from those in (a),(c),(e).

(The y component of the momentum flux is not addressed here because it is predicted to be zero by the WKB model.) Such a simple closed-form expression does not exist for the linear wind profile considered previously, since then the wave spectrum is not entirely affected by critical levels. Additionally, the exponential factor (51) then depends on the azimuthal angle θ [unlike (56)], and cannot be integrated analytically, so the momentum flux remains a 1D integral.

As can be seen, in linear conditions (i.e., $Nh_0/|\mathbf{U}_0| = 0.01$), the theoretical model does an excellent job of predicting this momentum flux up to $\mathrm{Ri}^{-1} = 3$, which surprisingly is in even better agreement than the surface drag for a similar range of Ri in, for example, TMV04. It should be stressed that both the term 5/(32Ri) and the term 1/(8Ri) inside the exponential in (59) (which are intrinsically WKB results) are essential to obtain such a good agreement. For higher values of $Nh_0/|\mathbf{U}_0|$, however, critical-level absorption is considerably weaker, with the momentum flux taking higher absolute values, especially, at low Ri. The numerical results for $Nh_0/|\mathbf{U}_0| = 0.1$ are still reasonably close to the WKB theoretical prediction over the whole range of Ri, but at $Nh_0/|\mathbf{U}_0| = 0.2$ the difference becomes large for $\mathrm{Ri}^{-1} > 2$, and at $Nh_0/|\mathbf{U}_0| = 0.5$ the same happens for $\mathrm{Ri}^{-1} > 1$. Curiously, at $\mathrm{Ri}^{-1} = 4$ the momentum flux is larger for $Nh_0/|\mathbf{U}_0| = 0.2$ than for $Nh_0/|\mathbf{U}_0| = 0.5$. This is likely to be due to saturation of the wave amplitude in the latter case, presumably associated with incipient wave breaking. This interpretation is confirmed by the fact that the value of the normalized surface drag for $Nh_0/|\mathbf{U}_0| = 0.5$ starts to decrease as Ri drops below 0.5 (not shown).

The agreement with nonlinear results would be improved slightly, but not substantially, if $\tilde{M}_x(z = \beta z/\pi)$ was normalized by the corresponding surface drag (which is generally higher in nonlinear conditions). This

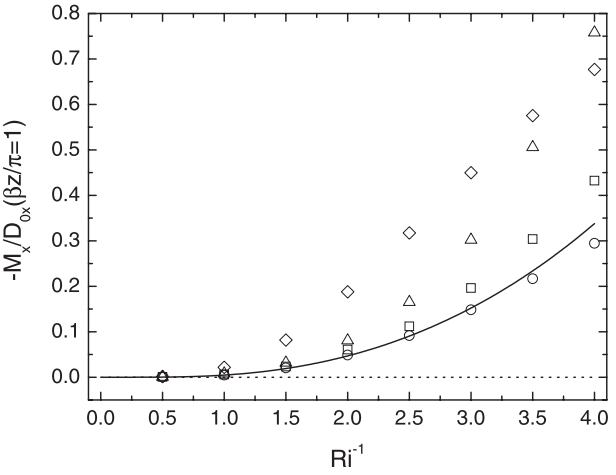

FIG. 5. Normalized momentum flux along x at $\beta z/\pi = 1$ for the wind profile (54) as a function of Ri^{-1}. Solid line: WKB model (59); dotted line: model of SG99; symbols: numerical results. Circles: $Nh_0/|\mathbf{U}_0| = 0.01$; squares: $Nh_0/|\mathbf{U}_0| = 0.1$; triangles: $Nh_0/|\mathbf{U}_0| = 0.2$; diamonds: $Nh_0/|\mathbf{U}_0| = 0.5$.

shows that discrepancies are not simply due to the different value of the momentum flux that is available to be absorbed, but also to the nature of the nonlinear absorption process itself (and possibly other phenomena, like wave reflection; see Breeding 1971). The model of SG99 (dotted line) would predict total momentum flux absorption in this situation, that is, $\tilde{M}_x(\beta z/\pi) = 0$.

4. Concluding remarks

The present study closes a series of papers (TMV04; Teixeira and Miranda 2004, 2006; Miranda et al. 2009) devoted to evaluating the effects of wind profile shear and curvature on mountain waves using a WKB approximation. Whereas previous papers have concentrated on the surface drag, the present paper focuses on the wave momentum flux. In this sense, it can also be viewed as an extension of the study of SG99 to lower Richardson numbers. The use of a WKB approximation enables the treatment of generic background wind profiles, as long as these profiles vary sufficiently slowly in the vertical, and are smooth enough below critical levels to preclude vertical wave reflections.

The effects of wind profile shear and curvature are of two types: first, the value of the surface drag (and of the momentum flux) may either be decreased (e.g., for a linear wind profile) or increased (e.g., for a wind that turns with height maintaining its magnitude). Second, for sufficiently low Ri, the momentum flux is not totally absorbed at critical levels, but rather filtered, with both the magnitude and phase of the waves changing (TMA08). For these effects to be captured correctly, and so that the momentum fluxes are accurate to second order in the small perturbation parameter used in the WKB approximation, it is necessary that the wave solutions are extended to third order.

This WKB model is only strictly valid in linear conditions and relatively weak shear, although it may probably be used for practical purposes for Ri as low as 0.5, as has been seen. Obviously, it is at these relatively low values of Ri that the model brings more substantial improvements with respect to the model of SG99. For the two wind profiles used to exemplify its capabilities, predictions from the WKB model are in good quantitative agreement with linear numerical simulations of the same flows (for $Nh_0/|\mathbf{U}_0| = 0.01$), especially when the finite horizontal extent of the domain is taken into account. Although it may be argued that deep layers with low Ri (such as were used to test the present model) seldom exist in nature, it should be stressed that the model is also applicable to more realistic wind profiles with variable Ri.

For the turning wind profile, there is a height where all the components in the wave spectrum have passed through their critical levels. The value of the momentum flux at this height constitutes a stringent test on the performance of the present model; namely, it assesses its ability to correctly represent wave attenuation by critical levels. Concerning this aspect, the performance of the model was seen to be very good in linear conditions for $\mathrm{Ri} \geq 1/3$.

Nonlinear effects considerably modify the behavior of the flow. In the weakly nonlinear cases considered here, the momentum fluxes are somewhat enhanced, but the linear predictions obtained using the WKB approximation retain their usefulness. For $Nh_0/|\mathbf{U}_0| = 0.1$ the WKB model is still useful quantitatively, whereas for $Nh_0/|\mathbf{U}_0| = 0.2$ and especially for $Nh_0/|\mathbf{U}_0 = 0.5$ its value is mainly qualitative, with its departures from the model of SG99 being, nevertheless, in the right direction. The momentum flux corrections due to shear effects, predicted by the model, correspond to a nonnegligible fraction of the uncorrected momentum fluxes, and are of the same order of magnitude as the corrections due to nonlinearity. This emphasizes their practical relevance.

Since the momentum flux divergence expressions found in this study are in closed analytical form, they should be easy to implement in gravity wave drag parameterization schemes. There are, admittedly, many improvements that could be made to the model presented here, including, for example, inclusion of the earth's rotation, nonhydrostatic effects, nonlinearity, boundary layer effects, or a differently shaped orography. This last improvement, which is particularly relevant for drag parameterization, appears to be the most feasible, for example, for the case of

an elliptical mountain (as in Teixeira and Miranda 2006). The other improvements are unlikely to be able to preserve the analytical simplicity of the approach employed here.

Acknowledgments. This work was supported by Fundação para a Ciência e Tecnologia (FCT) under Project AWARE/PTDC/CTE-ATM/65125/2006. The authors thank two anonymous referees for their useful comments, which have substantially improved this paper.

REFERENCES

Bacmeister, J. T., and R. T. Pierrehumbert, 1988: On high-drag states of nonlinear stratified flow over an obstacle. *J. Atmos. Sci.,* **45,** 63–80.

Bender, C. M., and S. A. Orszag, 1999: *Advanced Mathematical Methods for Scientists and Engineers*. Springer, 593 pp.

Booker, J. R., and F. P. Bretherton, 1967: The critical layer for internal gravity waves in a shear flow. *J. Fluid Mech.,* **27,** 513–539.

Breeding, R. J., 1971: A non-linear investigation of critical levels for internal atmospheric gravity waves. *J. Fluid Mech.,* **50,** 545–563.

Broad, A. S., 1995: Linear theory of momentum fluxes in 3-d flows with turning of the mean wind with height. *Quart. J. Roy. Meteor. Soc.,* **121,** 1891–1902.

Clark, T. L., and W. R. Peltier, 1984: Critical level reflection and the resonant growth of nonlinear mountain waves. *J. Atmos. Sci.,* **41,** 3122–3134.

Doyle, J. D., and Q. F. Jiang, 2006: Observations and numerical simulations of mountain waves in the presence of directional wind shear. *Quart. J. Roy. Meteor. Soc.,* **132,** 1877–1905.

Eliassen, A., and E. Palm, 1960: On the transfer of energy in stationary mountain waves. *Geofys. Publ.,* **22,** 1–23.

Garner, S. T., 2005: A topographic drag closure built on an analytical base flux. *J. Atmos. Sci.,* **62,** 2302–2315.

Gregory, D., G. J. Shutts, and J. R. Mitchell, 1998: A new gravity-wave-drag scheme incorporating anisotropic orography and low-level wave breaking: Impact upon the climate of the UK meteorological office unified model. *Quart. J. Roy. Meteor. Soc.,* **124,** 463–493.

Grubišić, V., and P. K. Smolarkiewicz, 1997: The effect of critical levels on 3d orographic flows: Linear regime. *J. Atmos. Sci.,* **54,** 1943–1960.

Keller, T. L., 1994: Implications of the hydrostatic assumption on atmospheric gravity waves. *J. Atmos. Sci.,* **51,** 1915–1929.

Kim, Y. J., S. D. Eckermann, and H. Y. Chun, 2003: An overview of the past, present and future of gravity-wave drag parametrization for numerical climate and weather prediction models—Survey article. *Atmos.–Ocean,* **41,** 65–98.

Leutbecher, M., 1998: Die ausbreitung orographisch angeregter schwerewellen in die stratosphäre (The propagation of orographic gravity waves into the stratosphere). Ph.D. thesis, Lugwig-Maximilians-Universität, Munchen, Germany, 167 pp.

Lin, Y.-L., 2007: *Mesoscale Dynamics*. Cambridge University Press, 674 pp.

Lindzen, R. S., 1981: Turbulence and stress owing to gravity wave and tidal breakdown. *J. Geophys. Res.,* **86,** 9707–9714.

Lott, F., and M. J. Miller, 1997: A new subgrid-scale orographic drag parametrization: Its formulation and testing. *Quart. J. Roy. Meteor. Soc.,* **123,** 101–127.

McFarlane, N. A., 1987: The effect of orographically excited graivty-wave drag on the general circulation of the lower stratosphere and troposphere. *J. Atmos. Sci.,* **44,** 1775–1800.

Miles, J. W., and H. E. Huppert, 1969: Lee waves in a stratified flow. Part 4: Perturbation approximation. *J. Fluid Mech.,* **35,** 497–525.

Miranda, P. M. A., and I. N. James, 1992: Non-linear three dimensional effects on the wave drag: Splitting flow and breaking waves. *Quart. J. Roy. Meteor. Soc.,* **118,** 1057–1081.

——, J. P. A. Martins, and M. A. C. Teixeira, 2009: Assessing wind profile effects on the global atmospheric torque. *Quart. J. Roy. Meteor. Soc.,* **135,** 807–814.

Ólafsson, H., and P. Bougeault, 1996: Nonlinear flow past an elliptic mountain ridge. *J. Atmos. Sci.,* **53,** 2465–2489.

Palmer, T. N., G. J. Shutts, and R. Swinbank, 1986: Alleviation of a systematic westerly bias in general circulation and numerical weather prediction models through an orographic gravity wave drag parametrization. *Quart. J. Roy. Meteor. Soc.,* **112,** 1001–1039.

Phillips, D. S., 1984: Analytical surface pressure and drag for linear hydrostatic flow over three-dimensional elliptical mountains. *J. Atmos. Sci.,* **41,** 1073–1084.

Shutts, G., 1995: Gravity-wave drag parametrization over complex terrain: The effect of critical-level absorption in directional wind-shear. *Quart. J. Roy. Meteor. Soc.,* **121,** 1005–1021.

——, and A. Gadian, 1999: Numerical simulations of orographic gravity waves in flows which back with height. *Quart. J. Roy. Meteor. Soc.,* **125,** 2743–2765.

Smith, R. B., 1979: The influence of mountains on the atmosphere. *Advances in Geophysics,* Vol. 21, Academic Press, 87–230.

——, 1986: Further development of a theory of lee cyclogenesis. *J. Atmos. Sci.,* **43,** 1582–1602.

Teixeira, M. A. C., and P. M. A. Miranda, 2004: The effect of wind shear and curvature on the gravity wave drag produced by a ridge. *J. Atmos. Sci.,* **61,** 2638–2643.

——, and ——, 2006: A linear model of gravity wave drag for hydrostatic sheared flow over elliptical mountains. *Quart. J. Roy. Meteor. Soc.,* **132,** 2439–2458.

——, ——, and M. A. Valente, 2004: An analytical model of mountain wave drag for wind profiles with shear and curvature. *J. Atmos. Sci.,* **61,** 1040–1054.

——, ——, J. L. Argain, and M. A. Valente, 2005: Resonant gravity-wave drag enhancement in linear stratified flow over mountains. *Quart. J. Roy. Meteor. Soc.,* **131,** 1795–1814.

——, ——, and ——, 2008: Mountain waves in two-layer sheared flows: Critical level effects, wave reflection and drag enhancement. *J. Atmos. Sci.,* **65,** 1912–1926.